Core−Shell Hematite Nanorods: A Simple Method To Improve the Charge Transfer in the Photoanode for Photoelectrochemical Water Splitting

Gurudayal,[†] Png Mei Chee,[†] Pablo P. Boix,*[,‡] Hu Ge,[†] Fang Yanan,[†] James Barber,*[,†,§,‖] and Lydia Helena Wong*[,†]

[†]Solar Fuels Lab, School of Materials Science and Engineering, Nanyang Technological University, 50 Nanyang Avenue, Singapore 639798

[‡]Energy Research Institute@NTU (ERI@N), Research Techno Plaza, X-Frontier Block, Level 5, 50 Nanyang Drive, Singapore 637553

[§]Applied Science and Technology Department—BioSolar Lab, Politecnico di Torino, Viale T. Michel 5, 15121 Alessandria, Italy

[‖]Department of Life Sciences, Imperial College London, London SW7 2AZ, United Kingdom

S *Supporting Information*

ABSTRACT: We report a simple method to produce a stable and repeatable photoanode for water splitting with a core−shell hematite (α-Fe2O3) nanorods system by combining spray pyrolysis and hydrothermal synthesis. Impedance spectroscopy revealed passivation of the surface states by the shell layer, which results in an increase of the charge injection through the hematite conduction band. In pristine hematite more holes are accumulated on the surface and the charge transfer to the electrolyte occurs through surface states, whereas in the core−shell hematite photoanode the majority of hole transfer process occurs through the valence band. As a result the photoactivity of the core−shell nanorods, 1.2 mA cm^{-2}, at 1.23 V vs RHE, is twice that of pristine hematite nanorods. The alteration of the interface energetics is supported by TEM, showing that the crystallinity of the surface has been improved by the deposition of the shell.

KEYWORDS: *hematite core−shell nanorods, photoelectrochemical water splitting, electrochemical impedance spectroscopy, incident photon to current conversion efficiency (IPCE), UV−vis absorption spectra, Mott−Schottky, hole scavenger*
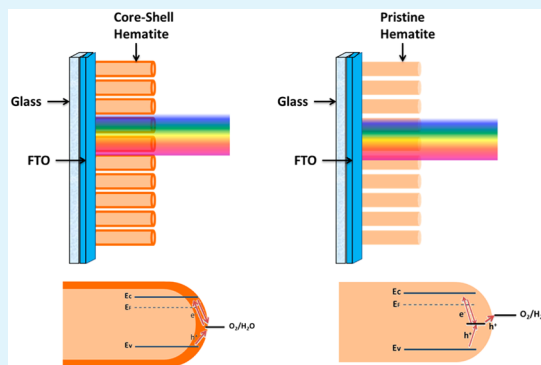
■ INTRODUCTION

Among the different ways of converting solar energy to useful forms of energy, artificial photosynthesis, in the form of photoelectrochemical (PEC) devices, offers a unique and simple way to store solar energy in the form of chemical bonds.[1−7] In this context, hematite (α-Fe$_2$O$_3$) has emerged as one of the most promising materials for the photoanode of a PEC system due to its promising energy band gap (2.0−2.2 eV), decent stability in aqueous solutions, and economic viability.[8,9] Fe$_2$O$_3$ has been expected to accomplish a theoretically STH efficiency of 16.8%.[10] However, the reported efficiencies are less than this estimation essentially due to the short photogenerated charge carriers lifetime, small hole diffusion length, sluggish oxygen evolution kinetics, and unfavorable conduction band potential with respect to the water reduction level, which requires an additional bias for hydrogen generation.[10−13]

To address these limitations, nanostructuring, doping, and surface treatment of hematite have been strategies explored.[14−24] Nanostructuring can be achieved by manipulating

various synthesis methods such as solution-based methods,[25] electrodeposition,[20] spray pyrolysis,[26] and APCVD.[23] Nanowire or nanorod arrays are favorable for attaining high photocurrent because the diameters can be tuned according to the hole diffusion length.[27,28] The hematite nanorods arrays have been synthesized previously by thermal oxidation of Fe foil and precipitation of Fe^{3+} from aqueous solution during hydrothermal synthesis.[28,29] Among these synthesis routes, hydrothermal precipitation of Fe$_2$O$_3$ is one of the simplest and most effective methods to grow large and uniform nanorods array.[27] We have successfully grown Fe$_2$O$_3$ nanorods array on FTO substrate and reported previously.[29] Hematite nanorods exhibited superior STH efficiencies than other nanostructures because of favorable [110] crystallographic orientation.[28] The main drawback of hematite is the requirement for an overpotential, which occurs due to the slow oxygen evolving
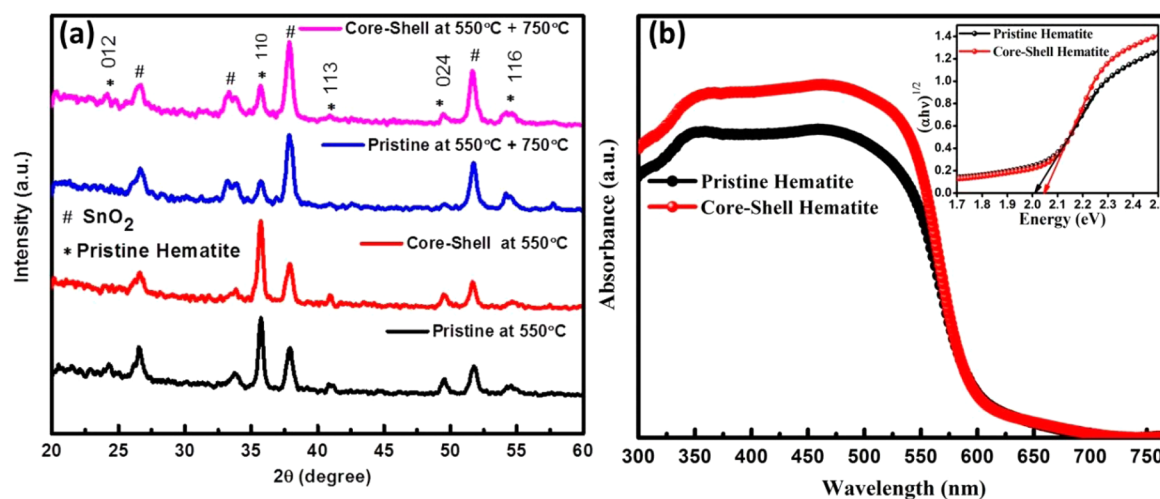
Figure 1. (a) XRD patterns of pristine hematite (α-Fe$_2$O$_3$) and core−shell hematite on FTO sample after annealing at 550 °C for 2 h and 750 °C for 20 min. The * denotes α-Fe$_2$O$_3$ (JCPDS 33-0664) and # denotes SnO$_2$ (JCPDS 46-1088), respectively. (b) UV−vis absorption spectra of pristine and core−shell hematite; inset shows the Tauc's plot.

reaction (OER) kinetics and the generation of surface trap states.[30,31] Surface treatment with OEC has been employed to overcome the OER kinetic issue, while surface passivation by various treatments has been shown to reduce the numbers of surface traps.[31−34] In addition, chemical alteration of the surface has also been reported to enhance the flat band potential and improve the optical absorption of Fe$_2$O$_3$.[35,36] In this article we demonstrate an inexpensive method to passivate surface defects by spraying a layer of hematite onto the pristine hydrothermally grown hematite nanorods, thus combining the nanostructuring effect with the surface passivation. We have investigated this system by electrochemical impedance spectroscopy (EIS) to elucidate the role of shell layer and the observed enhancement in the PEC performance. EIS revealed that the charge transfer to the electrolyte in pristine hematite nanorods occurs mainly through the surface states, whereas in core−shell hematite photoanodes it also takes place through the valence band due to the passivation of the surface states. TEM confirmed that the main reason underlying the different charge dynamics is the improved crystallinity due to the shell deposition.

■ EXPERIMENTAL PROCEDURE

The pristine and core−shell hematite nanorod samples were grown on a fluorine-doped tin oxide (FTO) substrate. The Fe$_2$O$_3$ nanorods were synthesized by modifying our previous method.[28] In short, after 6 h of hydrothermal synthesis at 100 °C, a uniform layer of FeOOH film was formed on the FTO substrate. The FeOOH samples were carefully rinsed with DI water. A 0.1 M iron acetylacetonate precursor in ethanol was sprayed onto the FeOOH nanorods with 4 cycles on hot plate at 525 °C for core−shell sample and finally annealed at 550 °C for 2 h to convert FeOOH to a hematite film. For photo-electrochemical measurements, pristine and core−shell photoanodes were again heated at 750 °C for 20 min.

■ CHARACTERIZATION AND MEASUREMENTS

X-ray diffraction patterns of pristine and core−shell Fe$_2$O$_3$ photoanodes obtained over a two theta value range from 20° to 60° with a Shimadzu instrument (Lab X, XRD-6000).

The surface morphology of the samples was characterized by FESEM (JEOL, JSM-7600F, 5 kV), while UV−vis absorption spectra of the hematite samples were obtained using a (PerkinElmer, Lambda 750S). The samples for TEM measurements were prepared by scraping the as-prepared electrode surface with a razor blade, which

only removed the hematite. Hematite was removed only from the same area as was analyzed in the photoelectrochemical, SEM, and XRD experiments. The scrapped hematite samples were transferred in to a vial with 2 mL of absolute ethanol, which was placed in a ultrasonicator for 30 s, and the hematite−ethanol mixture was dispersed onto a carbon-coated TEM grid. High-resolution trans-mission electron microscopy (HRTEM) image and selected area diffraction pattern (SADP) of hematite were investigated by JEOL 2100F TEM. Photoelectrochemical experiments were accomplished using CHI 660D working station (CH Instruments, Inc.) in a three-electrode system with 1 M NaOH (pH = 13.6) electrolyte under a light source of 150 W xenon solar simulator (67005, Newport Corp.) with an intensity equivalent to standard AM 1.5G sunlight (100 mW cm^{-2}) on the working electrode surface. The working electrode area was 0.12 cm^2. IPCE measurements have been done with a xenon light source (MAX-302, Asahi Spectra Co. Ltd.) coupled with a monochromator (CMS-100, Asahi Spectra Co. Ltd.) from a wavelength range of 300−600 nm, at a potential of 1.23 V vs RHE. The EIS analyses were carried out by a potentiostat (Methrohm-Autolab, AUT 83285) in a three-electrode electrochemical config-uration under 1 sun illumination. A potential perturbation (10 mV) was applied at varying dc voltages from −1 V to +1 V vs Ag/AgCl, with a frequency sweep from 200 kHz to 0.1 Hz. The impedance data was fitted by Z-view software. For Mott−Schottky plots, the capacitance was measured by applying a 10 mV perturbation at 1 kHz under dark conditions.

■ RESULTS AND DISCUSSION

The XRD patterns of the pristine hematite nanorods (grown hydrothermally) and core−shell hematite (hydrothermal growth followed by spray pyrolysis) photoanodes can be indexed to the characteristic peaks of Fe$_2$O$_3$ (JCPDS no. 003-0440), (Figure 1a). It is clear that the spray deposition of hematite precursor on pristine hematite nanorods does not generate any additional XRD peaks. The diffraction peak at 2θ = 35.8° indicates that Fe$_2$O$_3$ nanorods grow preferentially in the [110] direction, as previously reported.[27,28,37] This is a desired orientation for charge transport because this basal plane (001) shows four orders higher conductivity than the orthogonal plane, which improves the photo-oxidation kinetics. UV−vis spectra of pristine and core−shell hematite are shown in Figure 1b. The energy band gaps are nearly similar for both pristine and core−shell hematite photoanodes (inset, Figure 1b). The similar optical band gap of both samples (2.01 and
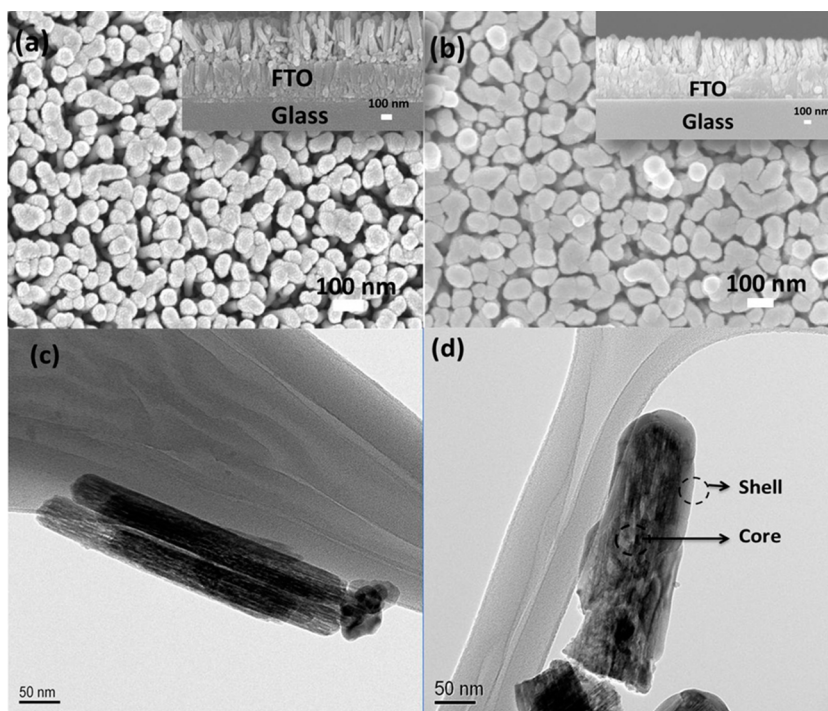
Figure 2. Top view FESEM images of (a) pristine hematite after annealing at 750 °C, (b) core−shell hematite after annealing at 750 °C, (c) TEM image of pristine hematite nanorod, and (d) TEM image of core−shell hematite.

2.04 eV for pristine and core−shell respectively) is consistent with the XRD results, which indicates no structural change occurs of Fe_2O_3 after spraying the hematite shell. The thicknesses of both the pristine and core−shell hematite samples are 350 and 370 nm, respectively, as seen in inset of Figure 2, and hence the optical absorption depth remains essentially the same as observed in UV−vis spectra.

Top view images from field emission scanning electron microscopy (FESEM) shown in Figures 2a and 2b reveal that pristine and core−shell hematite grown on the FTO substrate exhibit a nanorod organization, which remains unaffected with the deposition of the shell. Pristine hematite nanorods have the diameter of ∼60−80 nm, and the length is ∼360−380 nm. After a hematite shell is sprayed, the diameter of nanorods slightly increases to 80−100 nm and the length becomes 380−400 nm (Figure 2a and b). The best optimized thickness for hematite nanorods is 300−500 nm as we reported previously[27,28] because the absorption depth at 550 nm is around 200 nm.[18] In this work we investigated the effect of the core−shell structure in a fixed film thickness (350 nm). The composition of the pristine and core−shell hematite samples was analyzed by EDX line scan measurements along the interface of core and shell (Supporting Information Figures S3 and S4). As expected, the observed signals for Fe and O correspond to hematite. TEM image of the pristine hematite nanorods shows that these are about 60 and 350 nm in diameter and length, respectively, as indicated in Figure 2c. Figure 2d shows that the core−shell hematite possesses a conformal surface layer with a thickness of about 20 nm. An incremental change of 20% in the diameter of the core−shell nanorods, compared to the pristine hematite, is consistent with the FESEM results. In the pristine nanorod samples prepared by hydrothermal synthesis, water was used as a solvent which causes more residues on the surface. In the core−shell sample,

the shell layer was deposited using spray pyrolysis with ethanol as the solvent which results in a film with better crystallinity.

Photocurrent−voltage curves of core−shell hematite were found to give better performance compared to pristine samples (Figure 3a). The photocurrent density at 1.23 V vs RHE is 0.45 mA cm^{-2} for the pristine hematite nanorods sample and 1.20 mA cm^{-2} for core−shell sample. Before the dark current rises, a plateau of about 0.7 mA cm^{-2} is observed for the pristine sample, whereas the current increases to 2.6 mA cm^{-2} for core−shell hematite from 1.6 to 1.8 V vs RHE. This doubling of the photocurrent for the core−shell hematite photoanode at 1.23 V vs RHE is comparable with that obtained with hydrothermally grown 5% Mn treated hematite photoanode.[28] Photocurrent transient measurements were performed in order to observe the role of surface states at the pristine and core−shell hematite−electrolyte interface. The photoactivity with increasing bias voltage of both pristine and core−shell hematite photoanodes was measured with chopped illumination under AM 1.5G solar irradiance (Figure 3b). The positive transient in the photocurrent as the light is switched on indicates an accumulation of holes at the surface of the photoanode, caused by slow oxygen evolving reaction (OER) kinetics and trap surface states. Similarly, negative transients in the photocurrent are observed upon the light turnoff, which reflect that the photogenerated electrons recombine with the accumulated holes.

There is no transient current at high potentials, indicating that the injection barrier does not obstruct the holes transfer at the electrode/electrolyte interface.[23,38] At lower voltages, a small decrease in transients is observed for the core−shell hematite sample under illumination, while pristine sample clearly demonstrates greater transient behavior. This difference could be attributed to a variation in the total amount of accumulated holes at the photoanode−electrolyte interface, a commonly observed process in pristine hematite samples.
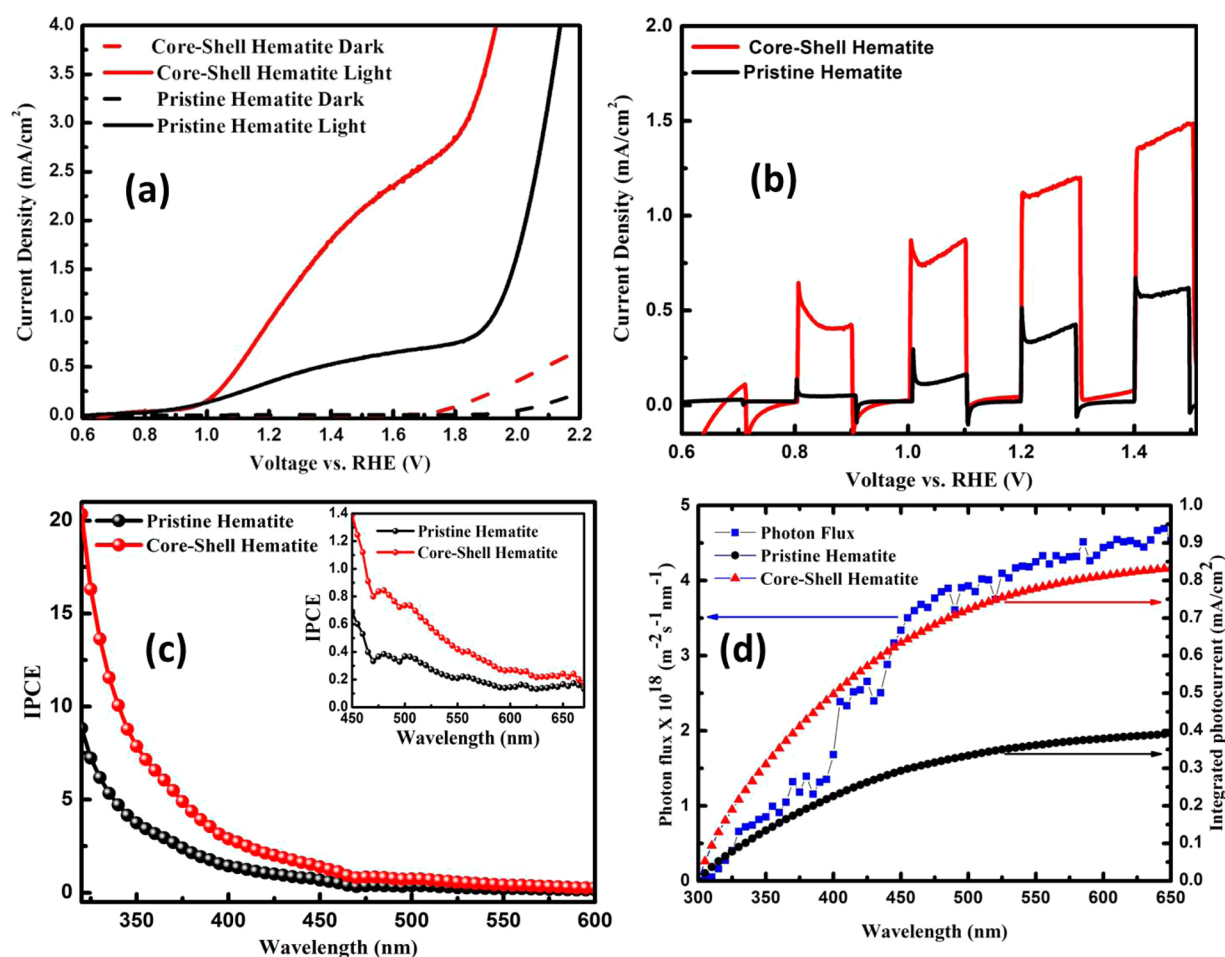
Figure 3. (a) Photocurrent−potential curve of pristine hematite photoanode and core−shell hematite measured under AM 1.5G 100 mW cm^{-2} in 1 M NaOH electrolyte solution. (b) Chopped photocurrent−potential curve of pristine hematite photoanode and core−shell hematite photoanodes. (c) IPCE spectra of pristine and core−shell hematite collected at 1.23 V vs RHE; inset shows the extrapolated IPCE from wavelength 450 to 650 nm. (d) Integrated photocurrent based on the IPCE data (300−650 nm); standard photon flux is shown as a reference.

To understand the relationship between the photoconductivity and light absorption of hematite photoanodes, we measured their performance as a function of wavelength of the incident light. IPCE measurements were performed on pristine and core−shell hematite nanorods at 1.23 V vs RHE (Figure 3c). IPCE can be calculated bu using the equation in previous reports.[4,15]

In comparison to pristine hematite photoanode, core−shell hematite photoanode shows higher photoconductivity over the entire spectral range. The IPCE drops to 0 after a wavelength of 600 nm, which is consistent with the hematite band gap energy.

Absorbed photon to current conversion (APCE) efficiency is shown in Supporting Information Figure S2, and core−shell hematite photoanode achieved higher collection and charge separation capability than pristine hematite. The integrated photocurrent density was calculated by the IPCE data with a standard AM 1.5G (100 mW cm^{-2}) photon flux by using the equation reported previously (see Supporting Information).[15,39]

The integrated photocurrents are 0.40 and 0.9 mA cm^{-2} for pristine and core−shell photoanodes, respectively (see Figure 3d), consistent with the measured photocurrent densities at 1.23 V vs RHE. It should be noted that the improved photocurrent of core−shell sample is not due to the photon

absorption because both samples show similar absorption spectra (Figure 1b).

In addition, after using a hole scavenger (H$_2$O$_2$), the current transients disappear and purely Faradaic photocurrents are observed in the complete potential range for pristine and core−shell hematite samples (Supporting Information Figure S6). This demonstrates that the injection barrier that is observed in the 1 M NaOH electrolyte is removed by the addition of 0.5 M H$_2$O$_2$. To understand the efficiency of hole injection at the hematite/electrolyte interface, the J−V curves of pristine and core−shell hematite photoanodes were measured with and without 0.5 M H$_2$O$_2$ (hole scavenger) under 1 sun (AM 1.5G) illumination. The photocurrent is found to double after adding 0.5 M H$_2$O$_2$ in 1 M NaOH electrolyte (Figure 4a and b). The charge separation and surface catalysis efficiency of pristine and core−shell samples are calculated (Figure 4c and d) by following a previous method reported by Dotan et al. (see the Supporting Information).[38] The charge separation efficiency starts to rise at a potential anodic to the flat band potential and saturate at 15% for pristine hematite and 30% for core−shell hematite at 1.23 V vs RHE (Figure 4c). The charge separation efficiency increases with the applied voltage because of the widening of the space charge layer. The higher charge separation efficiency of the core−shell hematite than the pristine nanorods indicates that the number of holes arriving at
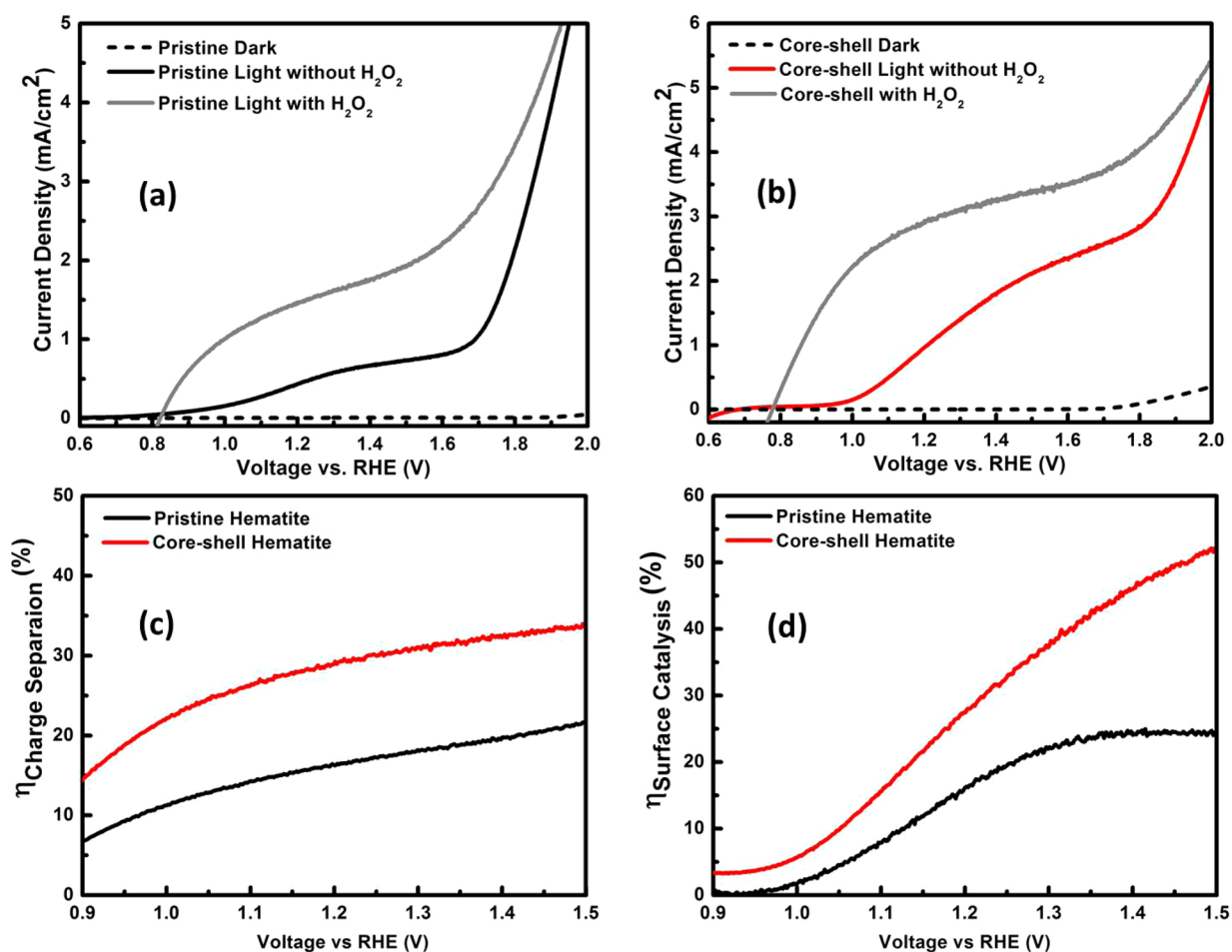
Figure 4. (a) Photocurrent−potential curve of pristine hematite photoanode measure under AM 1.5G in 1 M NaOH and 1 M NaOH with 0.5 M H_2O_2 electrolyte solution. (b) Photocurrent−potential curve of core−shell hematite photoanode measure under AM 1.5G in 1 M NaOH and 1 M NaOH with 0.5 M H_2O_2 electrolyte solution. (c) Charge separation efficiency of pristine and core−shell hematite photoanodes for water oxidation. (d) Surface catalysis efficiency of pristine and core−shell hematite for water oxidation.

the surface of the core−shell hematite is higher than those arriving at the surface of the pristine hematite. Therefore, the surface catalysis efficiency increases from 16% to 31% for core−shell hematite photoanode at 1.23 V vs RHE when using a H_2O_2 hole scavenger (Figure 4d). This shows that in the core−shell sample more holes are being injected to the electrolyte. Both of the observations (better hole transport and injection) show that the deposition of shell improves the quality of the hematite surface. The reasons behind this improvement were investigated by electrochemical impedance spectroscopy (EIS) and TEM.

Capacitance measurements of the pristine and core−shell hematite photoanodes at a frequency of 1 and 10 kHz are performed under dark conditions. The flat band potential and donor densities of pristine and core−shell hematite samples are calculated from the slopes of Mott−Schottky plots using the following equation:[13,40,41]

$$\frac{1}{C^2} = \left[\frac{2}{e\varepsilon\varepsilon_O N_d}\right]\left[V_A - V_{fb} - \frac{K_B T}{e}\right] \quad (1)$$

Pristine and core−shell hematite samples show a positive slope in the Mott−Schottky plots, which is expected from an n-type semiconductor (Figure 5a). The calculated donor densities are 8.19×10^{17} cm^{-3} and 1.39×10^{18} cm^{-3}. The flat band

potentials are 0.35 V vs RHE and 0.34 V vs RHE for pristine and core−shell hematite photoanodes, respectively.

EIS measurements were performed at different dc potentials under illumination. Although similar Nyquist plot patterns are obtained for both pristine and core−shell samples (Figure 5b, Supporting Information Figures S7, S8, and S9), the fitted data revealed different processes governing the performance of both kinds of systems. The pristine sample follows the trend corresponding to a charge transfer through surface states in good agreement with previous reports.[41] The characteristic fingerprint of this behavior is a peak of C_{trap} and a simultaneous valley of $R_{ct,trap}$ due to the filling of the surface states when the current is increasing, as shown in Figure 5c (where R_s represents the pure series resistance from the substrate and wires, $R_{trapping}$ is the resistance to fill the surface states, $R_{ct,trap}$ is the resistance to transfer the charge from the surface states to the electrolyte, and C_{bulk} and C_{trap} are the capacitances of the bulk and surface states, respectively (see equivalent circuit in the Supporting Information (Figure S1))). However, a different framework is obtained with the core−shell samples. The fitting of the results to the surface state charge transfer model does not result in the characteristics peak, pointing to a passivation of the surface states. In this situation, the charge transfer takes place mainly through the valence band, and the equivalent circuit is different ($R_{ct,trap}$ is simplified, and a new resistance accounting
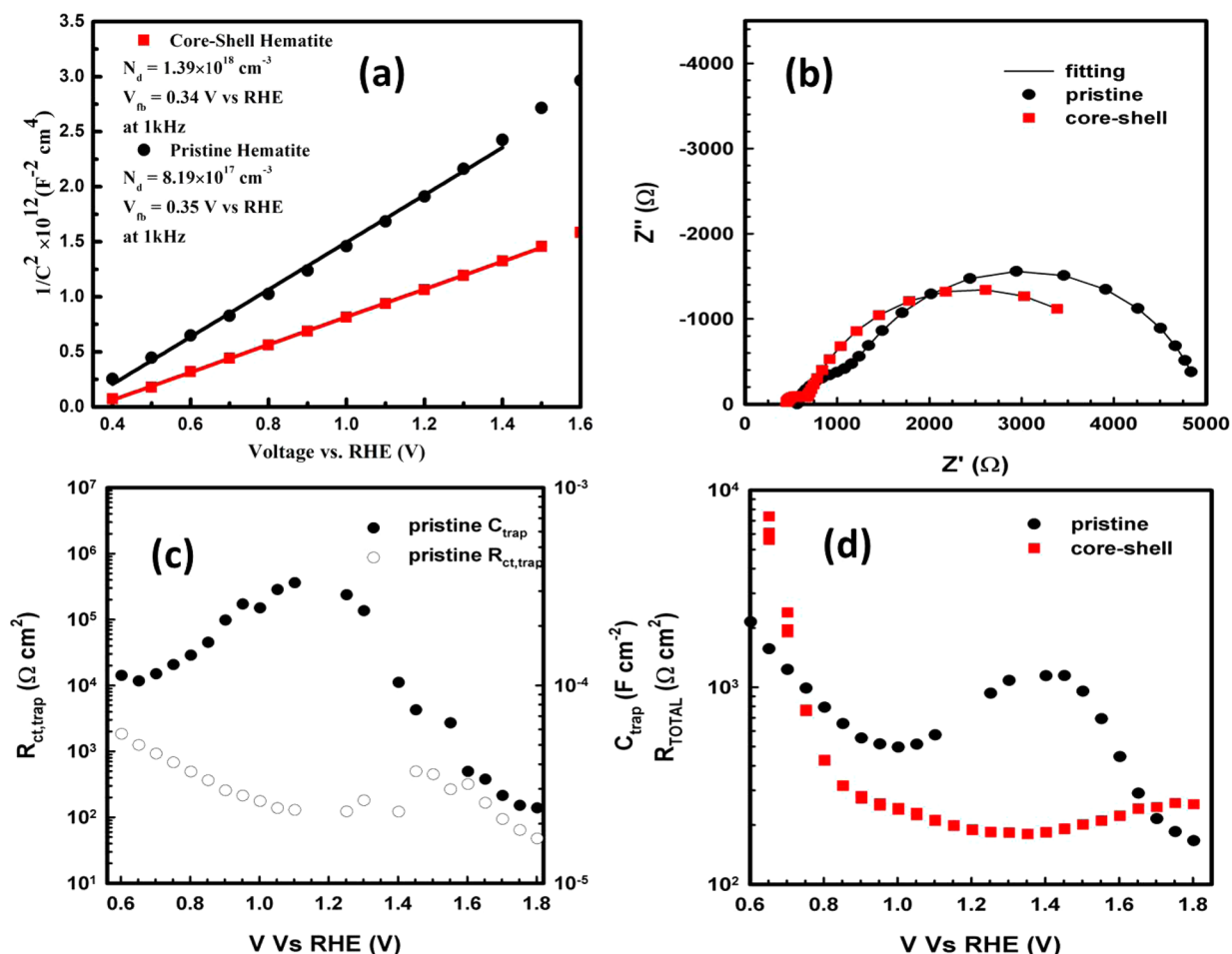
Figure 5. (a) Mott−Schottky plots of pristine (inset) and core−shell hematite extracted from EIS data measured at 1 kHz in the dark. Donor densities (N_d) and flat band potential (V_{fb}) extracted are shown in the figure. (b) Nyquist plots of pristine and core−shell hematite measured at pH 13.6 at 0.95 V vs RHE under 1 sun illumination. (c) Plots of equivalent circuit parameter $R_{ct,trap}$ obtained from fitting of EIS data under the illumination of 1 sun light and (d) R_{tot} values determined by the EIS fitting, where resistances associated with charge transfer.
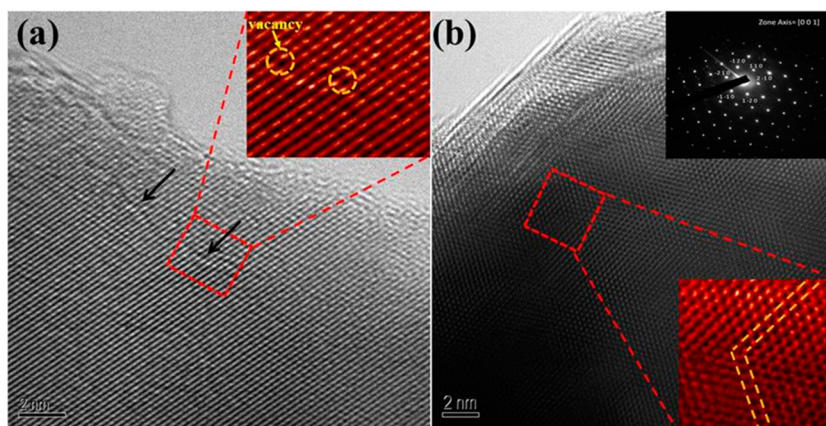

Figure 6. (a) HRTEM image of pristine nanorod showing the line defects by arrows and inset image showing the amplified image. (b) HRTEM image of core−shell hematite showing the good crystallinity without any line defects and inset image showing the inserted SAED pattern taken from [001] zone axis.

for the valence band charge transfer, $R_{ct,VB}$, is introduced in parallel to C_{bulk}; see the Supporting Information). The difference in the performance can be explained when the total resistance for the respective charge transfers ($R_s + R_{trapping} + R_{ct,trap}$ in the pristine case and $R_s + R_{ct,VB}$ in the core−shell case) are plotted (see Figure 5d). Despite the lower effective

surface area of the core−shell sample, its lower total charge transfer resistance results in a higher photocurrent. Therefore, we conclude that the charge transfer mechanism in the core−shell hematite structure is predominantly occurring through the valence band, which is most likely due to the passivation of the surface states. This reduction of the surface states is supported

by the current transients (Figure 3b), where the transient behavior is strongly reduced for the core—shell samples—in particular at higher voltages. At lower potentials, the traps still play a minor role; however, at higher potential the few remaining traps are filled and therefore they do not contribute to the transient.

The presence of different charge injection processes at the surface is in line with the HRTEM structural characterization. The HRTEM image of the pristine hematite sample (Figure 6a) shows a surface with poorer crystallinity as compared with the bulk of the hematite. This is also evident from the SAED pattern of this sample in Supporting Information Figure S5. The HRTEM image of the core—shell hematite sample (Figure 6b) shows a surface with better crystallinity as compared to the pristine hematite nanorods (Figure 6a), supporting the proposed surface states passivation. The SAED pattern (inset of Figure 6b) of the core—shell sample also reveals the good crystalline nature of this sample. The improvement in the crystallinity may originate from the diffusion of the Fe^{3+} ions from shell to the core of hematite during the high-temperature spray of the shell (525 °C). Therefore, it is proposed that the presence of the thin hematite shell not only improves the surface uniformity of the core—shell architecture but also improves the crystallinity and possibly passivates the surface states. As a result, the core—shell sample exhibits better charge transfer and surface catalytic properties, leading to superior photoelectrochemical properties.

CONCLUSIONS

To summarize, we have established a hydrothermal method to synthesize nanorods of pristine and core—shell hematite photoanodes. As compared to the pristine hematite nanorods, the core—shell structures were found to have an improved photoassisted water splitting activity. The core—shell hematite photoanode can improve the photocurrent densities by 2.5 times at 1.23 V vs RHE compared to the pristine hematite. The core—shell hematite also show higher charge separation and surface catalytic efficiency. Systematic evaluations were carried out to investigate the role of the hematite shell layer. EIS and TEM measurements reveal the beneficial effects of surface layer (shell), in particular the passivation of surface states and consequent charge injection through the valence band rather than through the surface states. Finally, the EIS analysis presented herein can also be used to analyze the role of other surface passivation layer on semiconductor photoanodes for PEC water splitting devices.

ASSOCIATED CONTENT

Ⓢ Supporting Information

Further measurement of analysis, EIS calculations, EDX spectra, Nyquist plots, APCE, transient current, and PEC data. This material is available free of charge via the Internet at http://pubs.acs.org.

AUTHOR INFORMATION

Corresponding Authors
*E-mail: PBPABLO@ntu.edu.sg.
*E-mail: j.barber@imperial.ac.uk.
*E-mail: Lydiawong@ntu.edu.sg.

Notes

The authors declare no competing financial interest.

REFERENCES

(1) Fujishima, A.; Honda, K. Electrochemical Photolysis of Water at a Semiconductor Electrode. *Nature* **1972**, *238*, 37—38.

(2) Butler, M. A.; Ginley, D. S. Principles of Photoelectrochemical, Solar Energy Conversion. *J. Mater. Sci.* **1980**, *15*, 1—19.

(3) Kennedy, J. H.; Frese, K. W., Jr. Photo-Oxidation of Water at Alpha-Fe_2O_3 Electrodes. *J. Electrochem. Soc.* **1978**, *125*, 709—714.

(4) Grätzel, M. Photoelectrochemical Cells. *Nature* **2001**, *414*, 338—344.

(5) Bak, T.; Nowotny, J.; Rekas, M.; Sorrell, C. C. Photo-Electrochemical Hydrogen Generation from Water Using Solar Energy. Materials-Related Aspects. *Int. J. Hydrogen Energy* **2002**, *27*, 991—1022.

(6) Walter, M. G.; Warren, E. L.; McKone, J. R.; Boettcher, S. W.; Mi, Q.; Santori, E. A.; Lewis, N. S. Solar Water Splitting Cells. *Chem. Rev.* **2010**, *110*, 6446—6473.

(7) Tachibana, Y.; Vayssieres, L.; Durrant, J. R. Artificial Photosynthesis for Solar Water-Splitting. *Nat. Photonics* **2012**, *6*, 511—518.

(8) Kennedy, J. H.; Frese, K. W., Jr. Flatband Potential and Donor Density of Polycrystalline Alpha-Fe_2O_3 Determined from Mott—Schottky Plots. *J. Electrochem. Soc.* **1978**, *125*, 723—726.

(9) Bassi, P. S.; Gurudayal; Wong, L. H.; Barber, J. Iron Based Photoanodes for Solar Fuel Production. *Phys. Chem. Chem. Phys.* **2014**, *16*, 11834—11842.

(10) Sivula, K.; Le Formal, F.; Grätzel, M. Solar Water Splitting: Progress Using Hematite (A-Fe_2O_3) Photoelectrodes. *ChemSusChem* **2011**, *4*, 432—449.

(11) Lin, Y.; Yuan, G.; Sheehan, S.; Zhou, S.; Wang, D. Hematite-Based Solar Water Splitting: Challenges and Opportunities. *Energy Environ. Sci.* **2011**, *4*, 4862—4869.

(12) Le Formal, F.; Tétreault, N.; Cornuz, M.; Moehl, T.; Grätzel, M.; Sivula, K. Passivating Surface States on Water Splitting Hematite Photoanodes with Alumina Overlayers. *Chem. Sci.* **2011**, *2*, 737—743.

(13) Kay, A.; Cesar, I.; Grätzel, M. New Benchmark for Water Photooxidation by Nanostructured A-Fe_2O_3 Films. *J. Am. Chem. Soc.* **2006**, *128*, 15714—15721.

(14) Balko, B. A.; Clarkson, K. M. The Effect of Doping with Ti(IV) and Sn(IV) on Oxygen Reduction at Hematite Electrodes. *J. Electrochem. Soc.* **2001**, *148*, E85—E91.

(15) Murphy, A. B.; Barnes, P. R. F.; Randeniya, L. K.; Plumb, I. C.; Grey, I. E.; Horne, M. D.; Glasscock, J. A. Efficiency of Solar Water Splitting Using Semiconductor Electrodes. *Int. J. Hydrogen Energy* **2006**, *31*, 1999—2017.

(16) Glasscock, J. A.; Barnes, P. R. F.; Plumb, I. C.; Savvides, N. Enhancement of Photoelectrochemical Hydrogen Production from Hematite Thin Films by the Introduction of Ti and Si. *J. Phys. Chem. C* **2007**, *111*, 16477—16488.

(17) Kleiman-Shwarsctein, A.; Hu, Y. S.; Forman, A. J.; Stucky, G. D.; McFarland, E. W. Electrodeposition of A-Fe_2O_3 Doped with Mo or Cr as Photoanodes for Photocatalytic Water Splitting. *J. Phys. Chem. C* **2008**, *112*, 15900—15907.

(18) Cesar, I.; Sivula, K.; Kay, A.; Zboril, R.; Grätzel, M. Influence of Feature Size, Film Thickness, and Silicon Doping on the Performance of Nanostructured Hematite Photoanodes for Solar Water Splitting. *J. Phys. Chem. C* **2009**, *113*, 772—782.

(19) Jang, J. S.; Lee, J.; Ye, H.; Fan, F.-R. F.; Bard, A. J. Rapid Screening of Effective Dopants for Fe_2O_3 Photocatalysts with Scanning Electrochemical Microscopy and Investigation of Their Photoelectrochemical Properties. *J. Phys. Chem. C* **2009**, *113*, 6719—6724.

(20) Kumar, P.; Sharma, P.; Shrivastav, R.; Dass, S.; Satsangi, V. R. Electrodeposited Zirconium-Doped A-Fe_2O_3 Thin Film for Photo-

electrochemical Water Splitting. *Int. J. Hydrogen Energy* **2011**, *36*, 2777−2784.

(21) Ling, Y.; Wang, G.; Wheeler, D. A.; Zhang, J. Z.; Li, Y. Sn-Doped Hematite Nanostructures for Photoelectrochemical Water Splitting. *Nano Lett.* **2011**, *11*, 2119−2125.

(22) Mao, A; Kim, J. K.; Shin, K.; Wang, D. H.; Yoo, P. G.; Han, G. Y.; Park, J. H. Hematite Modified Tungsten Trioxide Nanoparticle Photoanode for Solar Water Oxidation. *J. Power Sources* **2012**, *210*, 32−37.

(23) Le Formal, F.; Sivula, K.; Grätzel, M. The Transient Photocurrent and Photovoltage Behavior of a Hematite Photoanode under Working Conditions and the Influence of Surface Treatments. *J. Phys. Chem. C* **2012**, *116*, 26707−26720.

(24) Liao, P.; Carter, E. A. Hole Transport in Pure and Doped Hematite. *J. Appl. Phys.* **2012**, *112*, 17403−17413.

(25) Yang, Y.; Ma, H.; Zhuang, J.; Wang, X. Morphology-Controlled Synthesis of Hematite Nanocrystals and Their Facet Effects on Gas-Sensing Properties. *Inorg. Chem.* **2011**, *50*, 10143−10151.

(26) Xi, L.; Bassi, P. S.; Chiam, S. Y.; Mak, W. F.; Tran, P. D.; Barber, J.; Chye Loo, J. S.; Wong, L. H. Surface Treatment of Hematite Photoanodes with Zinc Acetate for Water Oxidation. *Nanoscale* **2012**, *4*, 4430−4433.

(27) Xi, L.; Tran, P. D.; Chiam, S. Y.; Bassi, P. S.; Mak, W. F.; Mulmudi, H. K.; Batabyal, S. K.; Barber, J.; Loo, J. S. C.; Wong, L. H. Co$_3$O$_4$-Decorated Hematite Nanorods as an Effective Photoanode for Solar Water Oxidation. *J. Phys. Chem. C* **2012**, *116*, 13884−13889.

(28) Gurudayal; Chiam, S. Y.; Kumar, M. H.; Bassi, P. S.; Seng, H. L.; Barber, J.; Wong, L. H. Improving the Efficiency of Hematite Nanorods for Photoelectrochemical Water Splitting by Doping with Manganese. *ACS Appl. Mater. Interfaces* **2014**, *6*, 5852−5859.

(29) Mulmudi, H. K.; Mathews, N.; Dou, X. C.; Xi, L. F.; Pramana, S. S.; Lam, Y. M.; Mhaisalkar, S. G. Controlled Growth of Hematite (A-Fe$_2$O$_3$) Nanorod Array on Fluorine Doped Tin Oxide: Synthesis and Photoelectrochemical Properties. *Electrochem. Commun.* **2011**, *13*, 951−954.

(30) Chou, J.-C.; Lin, S.-A.; Lee, C.-Y.; Gan, J.-Y. Effect of Bulk Doping and Surface-Trapped States on Water Splitting with Hematite Photoanodes. *J. Mater. Chem. A* **2013**, *1*, 5908−5914.

(31) Wheeler, D. A.; Wang, G.; Ling, Y.; Li, Y.; Zhang, J. Z. Nanostructured Hematite: Synthesis, Characterization, Charge Carrier Dynamics, and Photoelectrochemical Properties. *Energy Environ. Sci.* **2012**, *5*, 6682−6702.

(32) Bassi, P. S.; Gurudayal; Wong, L. H.; Barber, J. Iron Based Photoanodes for Solar Fuel Production. *Phys. Chem. Chem. Phys.* **2014**, *16*, 11834−11842.

(33) Peter, L. M.; Wijayantha, K. G. U.; Tahir, A. A. Kinetics of Light-Driven Oxygen Evolution at A-Fe$_2$O$_3$ Electrodes. *Faraday Discuss.* **2012**, *155*, 309−322.

(34) Pendlebury, S. R.; Cowan, A. J.; Barroso, M.; Sivula, K.; Ye, J.; Grätzel, M.; Klug, D. R.; Tang, J.; Durrant, J. R. Correlating Long-Lived Photogenerated Hole Populations with Photocurrent Densities in Hematite Water Oxidation Photoanodes. *Energy Environ. Sci.* **2012**, *5*, 6304−6312.

(35) Barroso, M.; Pendlebury, S. R.; Cowan, A. J.; Durrant, J. R. Charge Carrier Trapping, Recombination, and Transfer in Hematite (A-Fe$_2$O$_3$) Water Splitting Photoanodes. *Chem. Sci.* **2013**, *4*, 2724−2734.

(36) Xi, L.; Chiam, S. Y.; Mak, W. F.; Tran, P. D.; Barber, J.; Loo, S. C. J.; Wong, L. H. A Novel Strategy for Surface Treatment on Hematite Photoanode for Efficient Water Oxidation. *Chem. Sci.* **2013**, *4*, 164−169.

(37) Warren, S. C.; Voïtchovsky, K.; Dotan, H.; Leroy, C. M.; Cornuz, M.; Stellacci, F.; Hébert, C.; Rothschild, A.; Grätzel, M. Identifying Champion Nanostructures for Solar Water-Splitting. *Nat. Mater.* **2013**, *12*, 842−849.

(38) Dotan, H.; Sivula, K.; Gratzel, M.; Rothschild, A.; Warren, S. C. Probing the Photoelectrochemical Properties of Hematite (A-Fe$_2$O$_3$) Electrodes Using Hydrogen Peroxide as a Hole Scavenger. *Energy Environ. Sci.* **2011**, *4*, 958−964.

(39) Tsui, L. K.; Zangari, G. The Influence of Morphology of Electrodeposited Cu$_2$O and Fe$_2$O$_3$ on the Conversion Efficiency of Tio$_2$ Nanotube Photoelectrochemical Solar Cells. *Electrochim. Acta* **2013**, *100*, 220−225.

(40) Shimizu, K.; Lasia, A.; Boily, J. F. Electrochemical Impedance Study of the Hematite/Water Interface. *Langmuir* **2012**, *28*, 7914−7920.

(41) Klahr, B.; Gimenez, S.; Fabregat-Santiago, F.; Bisquert, J.; Hamann, T. W. Photoelectrochemical and Impedance Spectroscopic Investigation of Water Oxidation with "Co−Pi"-Coated Hematite Electrodes. *J. Am. Chem. Soc.* **2012**, *134*, 16693−16700.